Received: 14 August 2024 | Revised: 23 October 2024 | Accepted: 4 December 2024

DOI: 10.1002/mrm.30407

RESEARCH ARTICLE

Magnetic Resonance in Medicine

Ultra-high temporal resolution 4D angiography using arterial spin labeling with subspace reconstruction

Qijia Shen[1] | **Wenchuan Wu**[1] | **Mark Chiew**[1,2,3] | **Yang Ji**[1] | **Joseph G. Woods**[1] | **Thomas W. Okell**[1]

[1]Wellcome Centre for Integrative Neuroimaging, FMRIB, Nuffield Department of Clinical Neurosciences, University of Oxford, Oxford, UK

[2]Physical Sciences, Sunnybrook Research Institute, Toronto, Ontario, Canada

[3]Department of Medical Biophysics, University of Toronto, Toronto, Ontario, Canada

Correspondence
Qijia Shen, WIN/FMRIB Centre, John Radcliffe Hospital, Headley Way, Headington, Oxford, OX3 9DU, UK.
Email: qijia.shen@ndcn.ox.ac.uk

Funding information
NIHR Oxford Biomedical Research Centre, Grant/Award Number: NIHR203316; Royal Academy of Engineering, Grant/Award Number: RF\201819\18\92; Canada Research Chairs; Wellcome Trust, Grant/Award Numbers: 203139/Z/16/Z, 220204/Z/20/Z

Abstract

Purpose: To achieve ultra-high temporal resolution non-contrast 4D angiography with improved spatiotemporal fidelity.

Methods: Continuous data acquisition using 3D golden-angle sampling following an arterial spin labeling preparation allows for flexibly reconstructing 4D dynamic angiograms at arbitrary temporal resolutions. However, k-space data is often temporally "binned" before image reconstruction, negatively affecting spatiotemporal fidelity and limiting temporal resolution. In this work, a subspace was extracted by linearly compressing a dictionary constructed from simulated curves of an angiographic kinetic model. The subspace was used to represent and reconstruct the voxelwise signal timecourse at the same temporal resolution as the data acquisition without temporal binning. Physiological parameters were estimated from the resulting images using a Bayesian fitting approach. A group of eight healthy subjects were scanned and the in vivo results reconstructed by different methods were compared. Because of the difficulty of obtaining ground truth 4D angiograms with ultra-high temporal resolution, the in vivo results were cross-validated with numerical simulations.

Results: The proposed method enables 4D time-resolved angiography with much higher temporal resolution (14.7 ms) than previously reported (~50 ms) while maintaining high spatial resolution (1.1 mm isotropic). Blood flow dynamics were depicted in greater detail, thin vessel visibility was improved, and the estimated physiological parameters also exhibited more realistic spatial patterns with the proposed method.

Conclusion: Incorporating a subspace compressed kinetic model into the reconstruction of 4D ASL angiograms notably improved the temporal resolution and spatiotemporal fidelity, which was subsequently beneficial for accurate physiological modeling.

KEYWORDS

angiography kinetic model, arterial spin labeling, dynamic angiography, subspace reconstruction

1 | INTRODUCTION

Visualizing blood flow through the vessels in the brain provides valuable information for both diagnosis of many cerebrovascular diseases (e.g., stroke,[1] arteriovenous malformation,[2] and steno-occlusive disease[3]) and surgical planning.[4] X-ray–based methods (e.g., digital subtraction angiography) are widely used for assessment of vascular disease, yet exposure to radiation is known to carry some risk. Although contrast-based MRI methods are radiation free, there is some concern about the use of gadolinium contrast agent exposure and accummulation.[5–7] Being one of the standard methods for neurovascular imaging, time-of-flight (TOF) MRA acquires high spatial resolution blood vessel images without contrast agent. However, it is unable to provide hemodynamic information (e.g., to separate arterial and venous flow through an arteriovenous malformation) and provides poor depiction of small and slow-flowing vessels and can suffer from venous contamination.[8]

Another non-contrast–based method is arterial spin labeling (ASL),[9,10] which labels inflowing arterial blood by inverting the magnetization at a labeling plane. Taking the difference between images with and without labeling provides information about blood flowing in the arteries or into the tissue, depending on the post labeling delay (PLD) before image acquisition. Because static tissue signal is subtracted out, ASL images have zero background signal, which may enhance the visibility of small distal vessels.[11]

Further adding the information of how blood flow varies over time resulted in dynamic MRA, which provides much richer information for clinical diagnosis[12] and allows for the fitting of physiological models, providing quantitative metrics that could be sensitive to pathology.[13] Numerous methods have been developed recently to reconstruct time-resolved ASL angiograms. Some methods seek to encode temporal information into the ASL preparation process. Based on a Hadamard encoding scheme, the pseudo continuous ASL (PCASL)[9] pulse train can be separated into blocks with or without labeling at each repeat,[14,15] followed by only one readout[16] or a limited number readouts.[17,18] The time-resolved angiography information can then be reconstructed by "decoding" the resulting encoded images. Alternatively, a long train of temporally resolved readouts can be acquired immediately after each fixed labeling module to generate dynamic images.[11,19,20] High undersampling factors for each temporal frame is used to achieve high temporal resolution in short scan times. Advanced reconstruction methods can be adopted to leverage the complementary information available across multiple timepoints to mitigate undersampling artifacts. Song et al,[21] proposed k-space weighted image contrast (KWIC)[21] with radial sampling to reconstruct 4D dynamic MRA, which combined segmented spokes from different echoes at different parts of k-space. KWIC was later adopted in different dynamic MRA sequences.[20,22] Similarly, the keyhole method has also been exploited for time-resolved MRA[23] reconstruction to combine data with different contrast while reducing artifacts.

Despite sophisticated design for data combination, these methods averaged readouts acquired at different timepoints with different contrast to achieve sufficient k-space sampling. They not only limited the temporal resolution that dynamic MRA could achieve, but also affected the spatiotemporal fidelity of the reconstructed images, because different k-space samples are acquired with the labeled blood at different spatial locations, especially for vessels with fast transiting blood. Inevitably, obtaining dynamic MRA without averaging data across timepoints would dramatically increase the undersampling factor. To compensate for this, improved priors for the MR signal would need to be incorporated to improve the conditioning of the reconstruction problem.

In this work, we aim to reconstruct ultra-high temporal resolution 4D ASL angiography images. First, a kinetic model[13] describing the angiographic signal during the course of a series of readouts after each ASL preparation was introduced to simulate a set of physiologically plausible signal curves. Second, the subspace technique[24,25] was adopted to linearly compress this model and convert the poorly conditioned problem of reconstructing each time point into a better conditioned problem of estimating a small number of coefficient maps of these subspace components, greatly reducing the number of unknown variables and computational requirements. Third, as well as conventional 3D radial sampling, a previously developed cone trajectory[26] was integrated for efficient sampling of high spatial frequencies. Numerical simulations were performed to examine the spatiotemporal characteristics of our reconstruction and optimize the regularization weight. The in vivo data was acquired with a combined angiographic and perfusion sequence (CAPRIA)[27] but with only the angiogram reconstructed here. Altogether, high spatial resolution dynamic MRA images with temporal resolution equal to the sequence TR (~15 ms) were reconstructed. The physiological parameters estimated from the in vivo results were cross-validated with the numerical simulation for confirmation of the improvement in physiological modeling accuracy.

2 | METHODS

2.1 | Pulse sequence design

The pulse sequence used in this study was plotted in Figure 1. The sequence is composed of multiple repeats

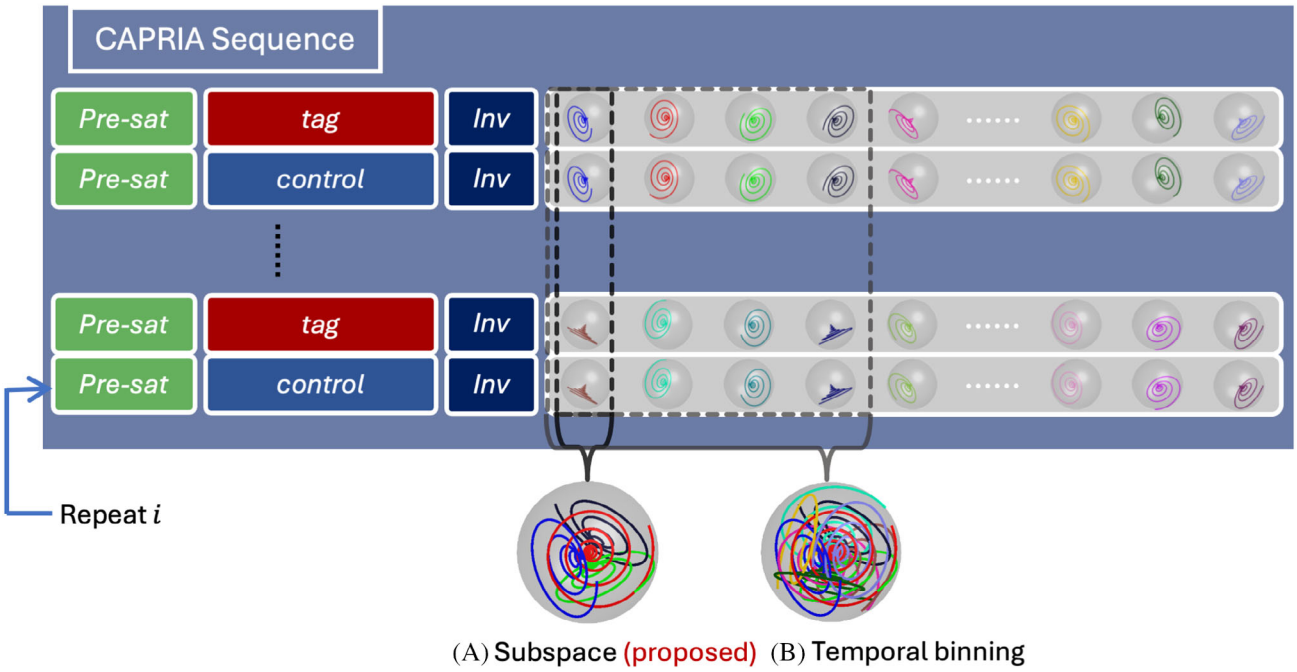

FIGURE 1 Overview of the CAPRIA pulse sequence with two different reconstruction methods. (A) In the proposed subspace method, each temporal frame contains only readouts at a single timepoint. (B) In contrast, in the temporal binning reconstruction scheme, each angiographic frame consists of readouts from several adjacent timepoints. As indicated by the blue arrow, each repeat has index i, and consists of pre saturation pulse (pre-sat), PCASL (tag for odd i, and control for even i), inversion and train of readouts. Note that in the radial protocol, each cone trajectory plotted in the figure would be replaced by a radial spoke aligned with its central axis.

where an identical PCASL preparation is used, but different k-space information is acquired. Within each repeat, a PCASL labeling or control module is followed by a single inversion pulse, as used in previous work[28] to help suppress background tissue signal, before a series of readouts are acquired. The PCASL labeling plane was placed within the neck in a similar manner to previous studies,[27] whereas the inversion pulse covered the whole imaging region. The details of the PCASL pulses are in Table S1. The direction of each readout spoke followed the 3D golden ratio,[29,30] the indices of which increased along the repeat dimension first as proposed by Song et al.[20] As an extension of the 2D golden angle,[30] the 3D golden ratio uses a fixed increment on both the azimuthal angle ($\alpha = 2\pi m\phi_1, \phi_1 \approx 0.6823$) and polar angle ($\beta = \arccos(m\phi_2), \phi_2 \approx 0.4656$) of the m^{th} readout spoke. Variable flip angles were applied to the train of readouts within each repeat to reduce the signal attenuation from the initial excitation pulses. In this work, two protocols were compared, one with a 3D radial trajectory and another with an in-house designed efficient cone trajectory.[26] The sequence design followed the combined angiographic and perfusion sequence[27] (CAPRIA), although here we only focus on the reconstruction of angiographic images.

To reconstruct a dynamic angiogram from the acquired data, conventionally, readouts from multiple TRs would be grouped to achieve sufficient k-space sampling, as shown in Figure 1B, which we term the "temporal binning" method. However, the proposed method, referred to as the "subspace" method in Figure 1A, combined spokes within only one TR for each frame, achieving a temporal resolution same as the TR. Further implementation details are explained below.

2.2 | Angiographic kinetic model

Given the sequence parameters (i.e., labeling duration, TR, flip angle, etc.), the angiographic signal evolution within each voxel after PCASL labeling was explicitly modeled by Okell et al,[13] with four independent parameters: the blood transit time from the labeling plane to the imaging voxel, δt; the sharpness, s; and time-to-peak, p, of a γ variate dispersion kernel, and a scaling factor proportional to blood volume, A. The model describing the signal variation across time is composed of effects from dispersion, relaxation, and attenuation because of RF pulses, which are explained below.

$D(t_d)$: the ideal temporal profile of the blood bolus is a rectangular function with a width equal to the labeling duration. Depending on the dispersion time-to-peak and sharpness, this ideal profile is blurred, which is described

by its convolution with a γ variate kernel, $D(t_d)$, while flowing through the vascular tree on the way to the voxel of interest, as described by Eq. ([1]). t_d is the transit time delay because of blood dispersion.

$$D(t_d) = \frac{s}{\Gamma(1+ps)} e^{-st_d}(st_d)^{ps}, (st_d > 0, ps > -1) \quad (1)$$

$T(\delta t, t_d)$: additionally, the inverted magnetization of blood experiences T_1 recovery as described by $T(\delta t, t_d)$ in Eq. (2). T_{1b} is the T_1 of arterial blood.

$$T(\delta t, t_d) = \exp\left(-\frac{\delta t + t_d}{T_{1b}}\right) \quad (2)$$

$R(t_d)$: the attenuation of the longitudinal magnetization difference signal by the imaging RF pulses is described by $R(t_d)$ in Eq. ([3]), making the simplifying assumption for this 3D acquisition that all labeled blood experiences all RF excitation pulses before t_d. TR is time for one RF pulse to the next in the train of readouts.

$$R(t_d) = \prod_1^n \cos(\alpha_i), \left(n = \left[\frac{t_d}{TR}\right]\right) \quad (3)$$

$S(t)$: finally, the actual signal amplitude depends on the flip angle at each excitation, contributing an additional $\sin(\alpha_i)$ term, as described previously.[27] Combining all these effects, the final signal profile S at each time after labeling t and each voxel position is characterized in Eq. ([4]).

$$S(t) = A\ \sin(\alpha_i) \int_{t-\delta t-\tau}^{t-\delta t} D(t_d)T(\delta_t, t_d)R(t_d)dt_d \quad (4)$$

2.3 | Subspace generation

The prior knowledge of the signal time series was incorporated into the reconstruction using a subspace method. Specifically, a plausible range of model parameters was chosen as follows: δt : 0.1~2.0 (second), p : 0.001~0.5 (second), s : 1~20 $\left(\text{second}^{-1}\right)$. (Note the parameter name s is different from second as a unit). To cover a wide range of temporal variations for blood flow, 40 equispaced samples were drawn for each parameter within the range and combined, forming a dictionary with 40^3 samples in total. The scaling factor A was not included in the dictionary generation process because it would not affect the subspace. As these different signal timecourses are strongly correlated with each other, they lie on a low-dimensional manifold embedded in a high-dimensional space. Although the exact manifold is not easy to find, a linear subspace can serve as a sufficient approximation, with straightforward calculation and computational convenience.[25] Singular value decomposition (SVD) was applied to the generated dictionary generating right singular vectors that are referred as principal components, as shown in Figure 2A. The space spanned by a small number of principal components was regarded as the subspace for the signal variation. As plotted in Figure 2B, the first few principal components capture slow signal variations, with higher order components containing more rapid oscillatory behavior. Using more principal components can give a better approximation to the signal variation, but requires higher computational cost. To determine the number of components required to strike a good balance between computational efficiency and accuracy, the relative error $\sqrt{\frac{\|X-\Phi\Phi^H X\|_F}{\|X\|_F}}$ was calculated on the whole dictionary, as shown in Figure 2C. X is the generated dictionary and Φ is the subspace. We found that using the first 12 components resulted in 0.961% relative error, and kept the number of unknown parameters same as reconstructing the 12 temporally binned frames.[26,27] The NRMSE at each timepoint is also shown in Figure 2D. Using 12 principal components achieved greatly reduced oscillatory errors compared to 4 or 8 components. Further increasing the number of components from 12 to 16 did not bring about significant improvements, but increased computational requirements. Therefore, 12 principal components were chosen for the subspace reconstruction for angiography in this work.

It is worth noting that the labeling efficiency of the PCASL module was not directly taken into account in the dictionary generation because it only changes the absolute scaling of the control-label magnetization difference at the start of the readout train, whereas the subspace was designed to describe the relative signal change during the readout train. The absolute scaling of the signal timecourse is reflected in the coefficient maps introduced below.

2.4 | Subspace reconstruction for angiographic images

The target time series, x, can be approximated by the weighted combination of principal components, Φ. As shown in Eq. (5), the voxelwise weights for each principal component, are to be estimated. The reconstruction problem was converted to the form of Eq. (6), where W_i was the i^{th} patch extraction operator, P was the sampling operator that interpolates the on-grid data after Fourier transform to the non-Cartesian trajectory, F was the Fourier transform and C were the coil sensitivity maps. y is the subtracted k-space data between tag and control, which share the same sampling trajectory. Similar to previous work,[25]

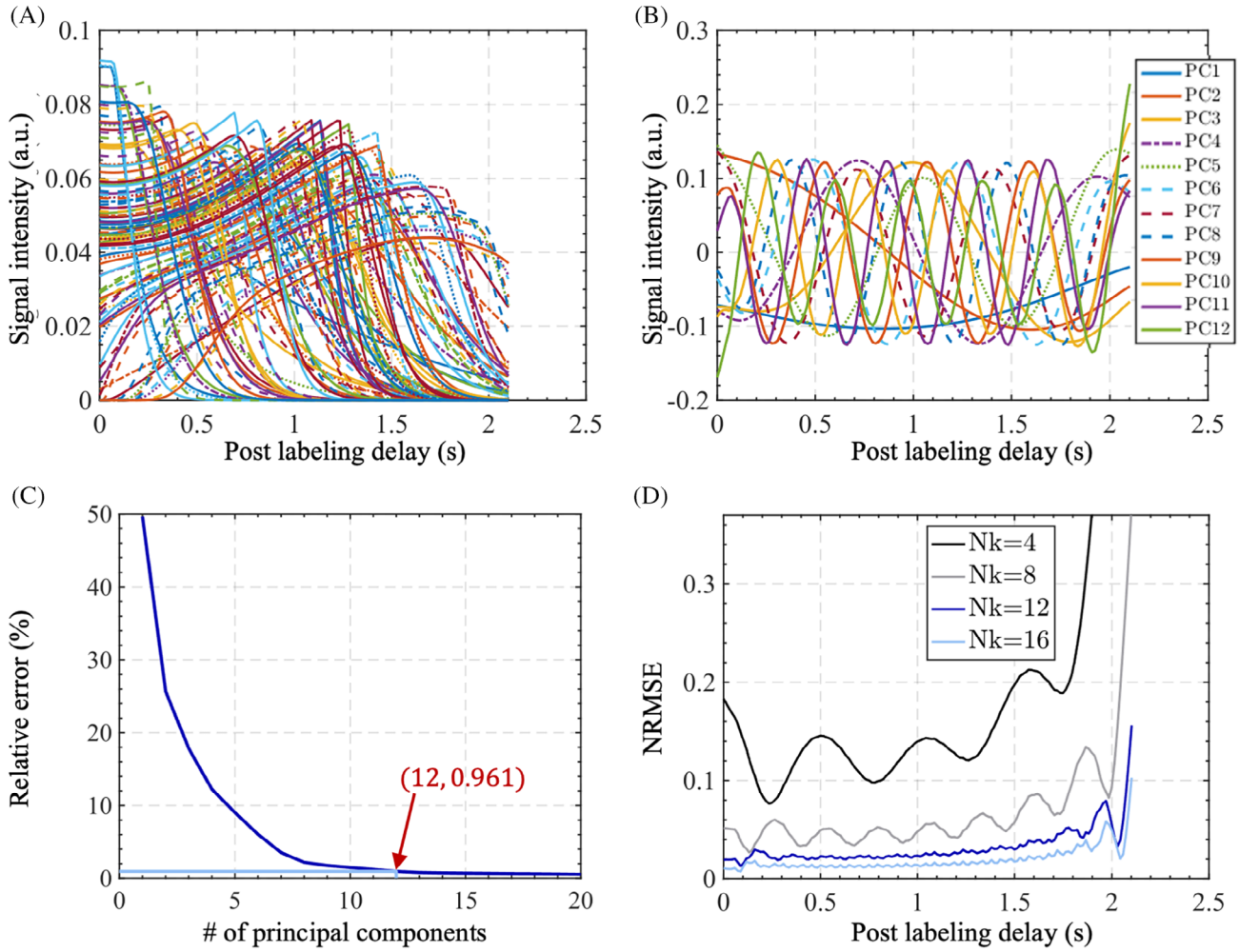

FIGURE 2 Subspace generation for the angiographic time series. (A) Simulated dictionary of angiographic time series across different combinations of plausible physiological parameters. (B) The first 12 orthogonal vectors in the right singular matrix denoted as principal components (PC) ~1–12 were extracted using singular value decomposition. Curves of PCs with larger indices manifest higher oscillating frequency. (C) Relative reconstruction error of the dictionary with different number of principal components used for angiography signal compression. (D) NRMSE at each timepoint with a different number (Nk) of principal components.

locally low rank (LLR) regularization[31] was applied across the principal component coefficient maps to reduce noise. λ was the weight adjusting the LLR regularization.

$$x \cong \Phi\alpha \tag{5}$$

$$\hat{\alpha} = \arg\min_{\alpha} \|PFC\Phi\alpha - y\| + \lambda \sum_{i} \|W_i(\alpha)\|_* \tag{6}$$

As operators F, C were applied on the spatial dimension, independent from the operator Φ on the temporal dimension, the original order of operators could be modified to $P\Phi FC\alpha$. The combined operator $\Phi^{\mathrm{H}}P\Phi$ used in every iteration could be calculated before the start of iterative optimization, therefore, the whole optimization process could be performed entirely in the subspace domain without expanding to a full time series.[25] The technique reduced the computation time of subspace reconstruction to that of the temporal binning reconstruction.

2.5 | Temporal binning reconstruction method

The proposed subspace reconstruction was compared against the method used to reconstruct 4D dynamic MRA in previous work.[26,27] As presented in Eq. ([7]), the LLR regularization was directly applied to the dynamic image x. Each frame involves grouped k-space data sampled from multiple TRs. Note the meaning of each notation was shared between Eqs. (6) and ([7]). The reconstruction was implemented in MATLAB 2023b (The MathWorks), except Extreme MRI, for which the official released code was used. The Michigan Image Reconstruction Toolbox[32] was used for non-Cartesian reconstruction and mapVBVD[33] was used for reading Siemens raw data.

$$\hat{x} = \arg\min_{x} \|PFCx - y\| + \lambda \sum_{i} \|W_i(x)\|_* \tag{7}$$

2.6 | Numerical simulation

Before in vivo acquisition, numerical simulations were performed to examine the spatiotemporal characteristics of the subspace reconstruction results compared to the original temporal binning reconstruction approach. A line with one voxel width crossing the center of every 3D volume and varying across time was created, simulating a time series of a single vessel. The four parameters of the kinetic model in Eq. ([4]) (i.e., $\delta t, p, s, A$) were distributed along the line in a linearly varying fashion, simulating increasing transit time and greater dispersion along the length of a vessel. Following the previous literature,[13] δt ranged between 0.25 and 1.8 s, p ranged between 0.1 and 0.5s, s ranged between 1 and 10s^{-1}, and the scaling parameter A was set to be equal to 1 along the simulated vessel. A 4D time series with the same spatial resolution (1.1 mm) as in vivo reconstruction was simulated with these parameters and the kinetic model. The TR, number of readouts and k-space trajectories in the simulation were also kept the same as for the in vivo acquisition protocols. After transforming the 4D time series to k-space with a single coil and uniform sensitivity using the minimum–maximum-based forward nonuniform fast Fourier transform (NUFFT),[34,35] temporal binning and subspace methods were used to separately reconstruct from the k-space data. To compare the spatial resolution, a point spread function was also calculated along the direction perpendicular to the simulated line. Both the radial trajectory used in Okell et al,[27,28] and the cone trajectory used in Shen et al[26] were simulated and reconstructed with the two methods. A variational Bayesian method (Fabber,[36] part of FMRIB Software Library[37]) was used to infer the four model parameters from the reconstructed images and evaluate the reconstruction quality. Additionally, weights $1 \times 10^{-4}, 5 \times 10^{-4}, 1 \times 10^{-3}$, and 1×10^{-2} for the LLR regularization term were tested for subspace reconstruction to inform the in vivo scenario. The data transformed from numerical phantom to k-space was scaled in the same way as described in in vivo scenario later before iterative reconstruction to ensure the regularization weight transferrable to in vivo reconstruction. To align with the optimal design in previous literature,[26,27] the regularization weight of 1e−1 was used for temporal binning reconstruction.

2.7 | In vivo acquisition and reconstruction protocols

To evaluate the proposed reconstruction method, a group of eight subjects (between 24- and 35-years old) were scanned on a 3 T Prisma scanner (Siemens Healthineers) using a 32-channel receive-only head coil under a technical development protocol agreed by local ethics and institutional committees, and they all provided consent.

For each subject, two back-to-back scans with two different protocols were acquired. The two protocols followed the same design as the "cone protocol" and "matched radial protocol" in the previous literature.[26] The variable flip angles varied quadratically across the readout and ranged between 3° to 12°. The TR for each readout was 14.7 ms, where the readout time was 10 ms. Note that the ASL labeling duration (1.8 s), the total time for all readouts after each ASL labeling module (2116.8 ms) as well as the total scan time (6 min 12 s) were kept consistent between the two protocols. The FOV was 200 mm × 200 mm × 125 mm, and the spatial resolution was 1.13 mm isotropically.

Before reconstruction, the original 32-channel data were compressed to eight virtual coils using principal component analysis (PCA)-based method.[38] The number of virtual coils after compression was kept consistent to the previous literature[26] and was empirically chosen to balance between computational requirements and reconstruction fidelity. Coil sensitivity map estimation used the adaptive combination method,[39] whose computation can be parallelized for acceleration. The data for reconstructing the last two frames of angiography was used for coil sensitivity estimation. However, instead of taking the difference between tag and control data, as was done for the angiography reconstruction, we took the mean of the tag and control data. A coil-wise pseudo-structural image was then reconstructed using the NUFFT from this mean data, which was then be used to estimate the coil sensitivities. For the temporal binning reconstruction, we followed previous literature[26] and used 1e−1 as the LLR regularization weight. For the subspace reconstruction, differences in data scaling between simulated and acquired data were removed by dividing both k-space data sets by their 95-percentile magnitude value before reconstruction to allow transfer of the fine-tuned regularization weight from numerical simulation to in vivo data. Based on the numerical simulation, a regularization weight of 5e−4 was adopted for subspace reconstruction.

Apart from the subspace and temporal binning reconstruction methods mentioned above, two advanced image reconstruction methods were also included for comparison, where the temporal resolution was matched to that of the subspace method. First, we adapted the LLR regularized reconstruction used by temporal binning to achieve the same temporal resolution as the subspace method, termed "LLR-matched" below. Another method "Extreme MRI,"[40] which combined multi-scale low rank and stochastic reconstruction, was also used for comparison. For both methods, different regularization weights

were investigated, the details of which are shown in Figures S1 and S2.

3 | RESULTS

3.1 | Numerical simulations

Simulated results on a single-vessel numerical phantom are shown in Figure 3. In the 4D phantom (Figure 3A), the blood bolus flows from left to right, with early blood arrival and minimal dispersion on the left and delayed arrival and greater dispersion moving to the right. The signal time series from three representative locations along the simulated vessel are displayed to compare the reconstruction fidelity between the subspace and temporal binning methods. Where the ground truth signal varies rapidly on the left of the phantom (early arrival and low dispersion), the subspace reconstruction cannot fully represent this rapid signal change and there is a slight discrepancy between the reconstructed signal and the ground truth. However, the subspace method still captures the overall signal trend. In contrast, the temporal binning signal curve drops from the beginning and fails to delineate the

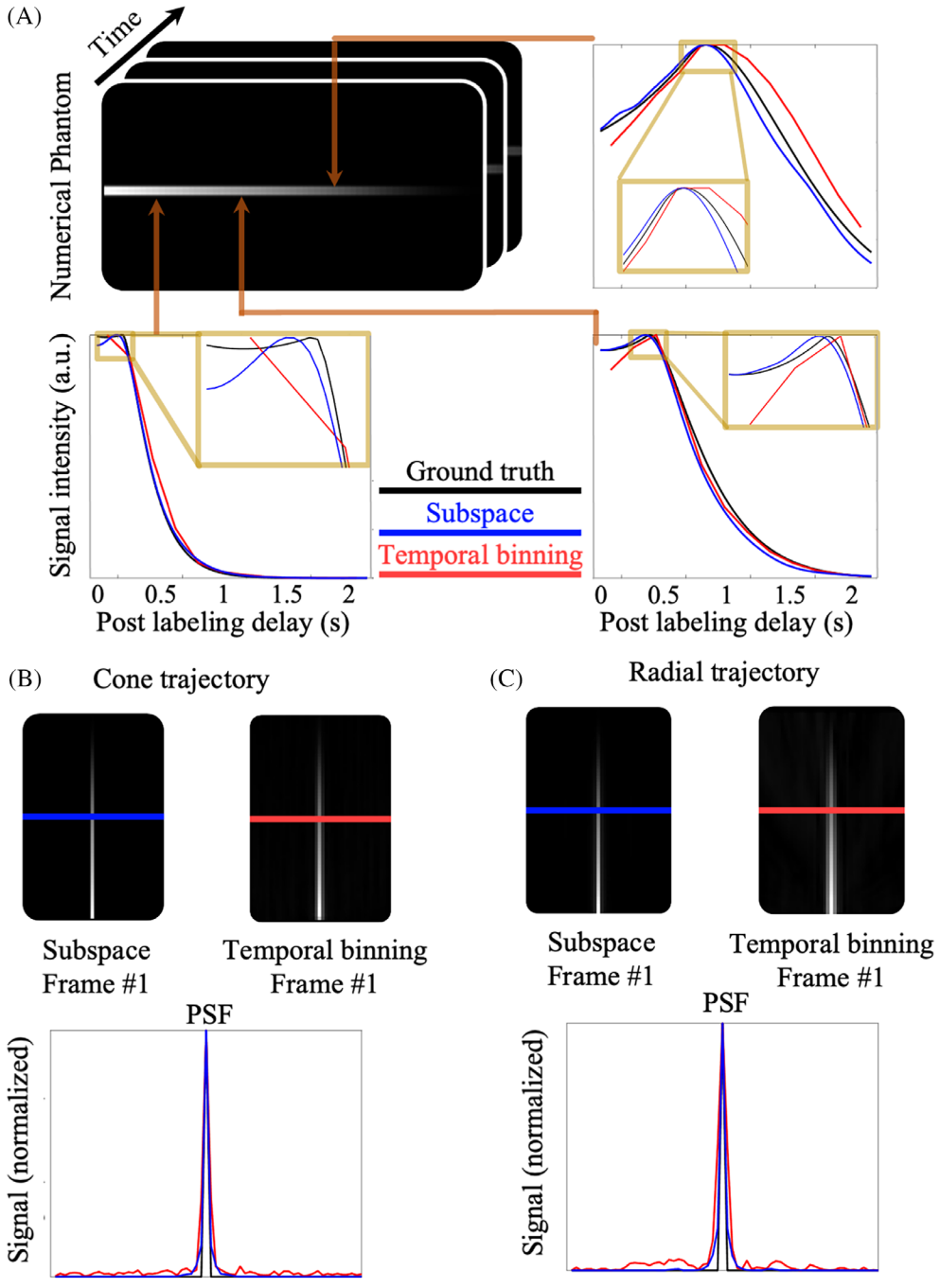

FIGURE 3 Spatiotemporal comparison of simulated results between the subspace and temporal binning reconstruction methods. (A) The signal timecourses sampled from three points along the simulated vessel are shown. The curves reconstructed using the subspace method approximated the "ground truth" with better accuracy. (B,C) The point spread function from the plane perpendicular to the simulated vessel using both cone (B) and radial (C) trajectories for the two reconstruction methods. Combined with cone and radial trajectories, the subspace method showed a thinner central lobe, lower sidelobe aliasing, and improved delineation of this narrow structure than temporal binning in both cases.

plateau and sharp transition because of averaging data points across a wide temporal window. Toward the middle and right of the phantom where the signal arrives later and is more dispersed, the subspace method gives a very good approximation to the ground truth signal, whereas the temporal binning result still deviates from the ground truth before the signal peak. Additionally, in the temporal binning results, when the peak time lies between two reconstructed frames the resulting signal curve shows a plateau rather than a single peak, as shown in Figure 3A.

In Figure 3B,C, the spatial characteristics of both reconstruction methods as well as both sampling trajectories were examined. The point spread function on the plane through the volume center and perpendicular to the line was plotted because the phantom was one voxel wide. In Figure 3B,C, regardless of the sampling trajectory, the central peak was thinner in the subspace point spread function than it was for temporal binning. The sidelobe aliasing was also better suppressed when using the subspace reconstruction approach compared to the original temporal binning method for both cone and radial trajectories.

Figure 4 shows how the improvement in the temporal fidelity of the reconstructed signal with the subspace approach translated into improved angiography parameter estimation. In Figure 4A, parameters estimated

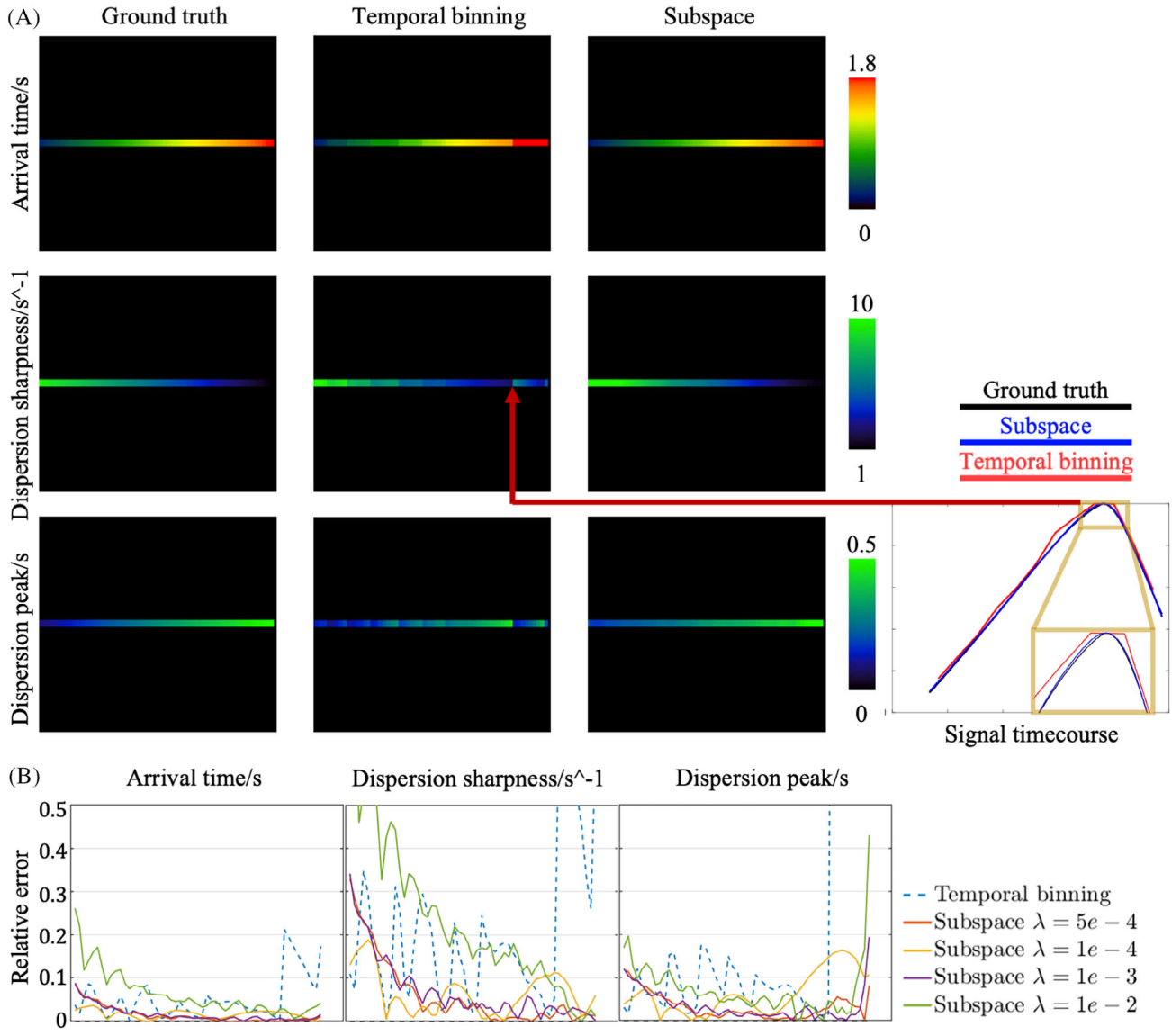

FIGURE 4 Parameter estimation from numerical phantom images reconstructed by subspace and temporal binning methods using the cone trajectory. (A) Comparison of estimated dispersion parameters and arrival time between the two methods. (B) Relative error of the estimated parameters along the simulated line compared to the ground truth. Parameters estimated from the subspace method with different regularization weights were explored.

with the temporal binning method exhibited a discrete and stepwise pattern, unlike the gradual variation in the ground truth image. As shown in the zoomed-in region in Figure 4A, one cause of these errors were when the true signal peak was not captured in the temporal binning reconstruction because of the limited temporal resolution. In comparison, the parameters estimated from the subspace approach were smoothly varying and closer to the ground truth. In Figure 4B, the relative error of the temporal binning and subspace methods with different regularization weights were plotted. It could be observed that parameters of temporal binning were mostly overestimated and deviated from the ground truth much further than the subspace results. In addition, the most accurate quantification was achieved when the regularization weight was set to 5e−4 in the subspace reconstruction, which was adopted for subspace reconstructions of the in vivo data below.

3.2 | In vivo angiography results

In vivo angiograms reconstructed with subspace and temporal binning methods are compared in Figures 5 and 6. Note that the vasculature was already filled with blood at PLD = 88 ms because a relatively long (1.8 s) labeling duration was used in the protocol.

The notable improvement in spatial fidelity could be observed in images reconstructed from data acquired with a radial trajectory (Figure 5). Consistent with the simulated results in Figure 3B, the angiograms generated by the subspace method show improved delineation of fine vessels compared to temporal binning. For instance, more vessels could be visualized with better clarity in the middle cerebral artery in subspace result compared to the temporal binning result, as shown in the enlarged blue box in the figure. The relative signal intensity of vessels compared to background was further investigated with line profiles, where the peak to bottom difference were noticeably larger in subspace data, indicating that vessels were more discernable from the background in the subspace reconstruction.

In Figure 6, the data acquired with the cone trajectory was also reconstructed with temporal binning and subspace approaches, respectively. Three consecutive frames in temporal binning angiography are shown in the first row. The subspace results have much higher temporal resolution than the temporal binning results. Between every two successive temporal binning frames, 10 more frames were reconstructed using the subspace method, demonstrating much smoother signal variations. Note, only one intermediate frame is shown here in Figure 6 for brevity. Regions around the internal carotid artery were zoomed in from each frame and the dynamic of blood flow was better depicted temporally in subspace method than in the temporal binning method. In addition, the spatial fidelity of MRA was also improved in the subspace approach compared to temporal binning as illustrated in the zoomed-in green regions.

3.3 | Quantitative comparison

The time-resolved MRA in vivo data reconstructed by the two different methods was further analyzed to extract physiological parameter maps (Figure 7). In agreement with the simulation results in Figure 4A, the in vivo arrival time estimated from temporal binning exhibited stepwise discontinuities along the arteries (Figure 7A), whereas the subspace data gave a more realistic smooth, continuous increase in transit time along the arteries, thanks to its ultra-high temporal resolution. The discontinuity of the estimated arrival time limited by the temporal resolution of the temporal binning approach also caused apparent asymmetry in the external carotids as marked by the cyan box. Such asymmetry was mitigated in the subspace result. Additionally, although there is no ground truth for this in vivo data, the arrival time appears to be over-estimated with temporal binning when the transit times are close to the length of the readout train (~2.1 s). This overestimation was observed in both simulated and in vivo results, exemplified in the white circle, but was noticeably improved in the subspace results. The blood dispersion parameters also benefited from the improved temporal resolution and fidelity available with the subspace method, as shown in Figure 7B. For instance, the dispersion sharpness of temporal binning MRA in the distal arteries was much higher than with the subspace reconstruction, which is inconsistent with previous work[13] and the expectation that dispersion will continue to increase as blood passes down the vascular tree. This observation was also consistent with the simulation results (yellow circle).

Parameter map histograms derived from the temporal binning and subspace reconstruction methods are shown in Figure 8, both for a single subject (Figure 8A) and for all subjects (Figure 8B). In both cases, the arrival time distribution for the temporal binning data showed discrete peaks, unlike the smoother distribution observed with the subspace data, most likely caused by the limited temporal resolution of the temporal binning data. As was observed in Figure 7, the dispersion sharpness appeared to be overestimated in temporal binning relative to the subspace approach. Although the dispersion peak was also likely biased in the temporal binning results based on our simulation results, the direction of deviation varied (Figure 4A).

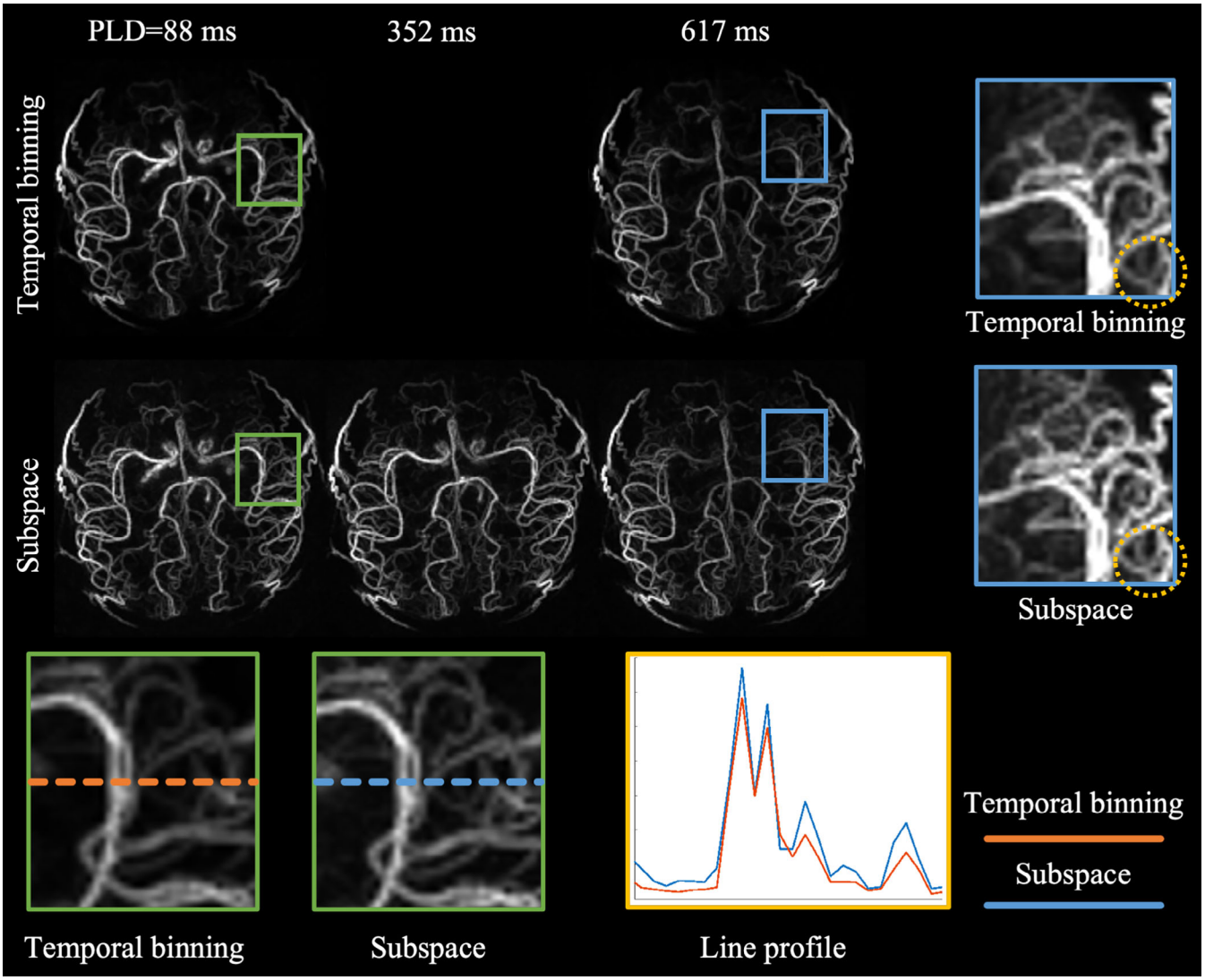

FIGURE 5 Spatial comparison of dynamic MRA acquired with a radial trajectory and reconstructed by subspace and temporal binning methods. Note that the vasculature was already filled with blood at PLD = 88 ms as a relatively long labeling during (1.8 s) was used. The quoted PLD represents the center of the temporal window for each frame. The temporal binning result did not have the image at PLD = 352 ms because of limited temporal resolution. Regions in the green box were zoomed for comparison of the visibility of thin vessels. Line profiles were sampled within the green box for both reconstruction methods. Regions enclosed in the blue box were also zoomed in to confirm the better visibility of vessels in the subspace results across time. The yellow circle marked an example where thin vessels were hard to distinguish from the background when using temporal binning but became much clearer when using the subspace approach. PLD, post-labeling delay.

3.4 | Comparison with other advanced reconstruction methods

In Figure 9, the angiography results were further compared against other advanced methods reconstructed with the same temporal resolution as the subspace method from the same k-space data. As all 144 frames were explicitly reconstructed, the LLR-matched approach had much higher computation time and memory requirements (300 GB memory, 28 h reconstruction time) than the subspace method (130 GB memory, 4 h reconstruction time). In addition, because 12× more frames were reconstructed than temporal binning without introducing additional regularization, LLR-matched exhibited degraded image quality and only the large arteries with strong signal intensity could be visualized, whereas the small distal vessels were lost, as shown in the green box. The reduced sampling per frame of LLR-matched also increased its dependence on locally low rank regularization, which introduced artifacts in arteries highlighted by the red arrow. Extreme MRI used an even more sophisticated reconstruction with multi-scale low rank patches and resulted in better sharpness of small vessels than LLR-matched. However, SNR was low and image details were inferior to those

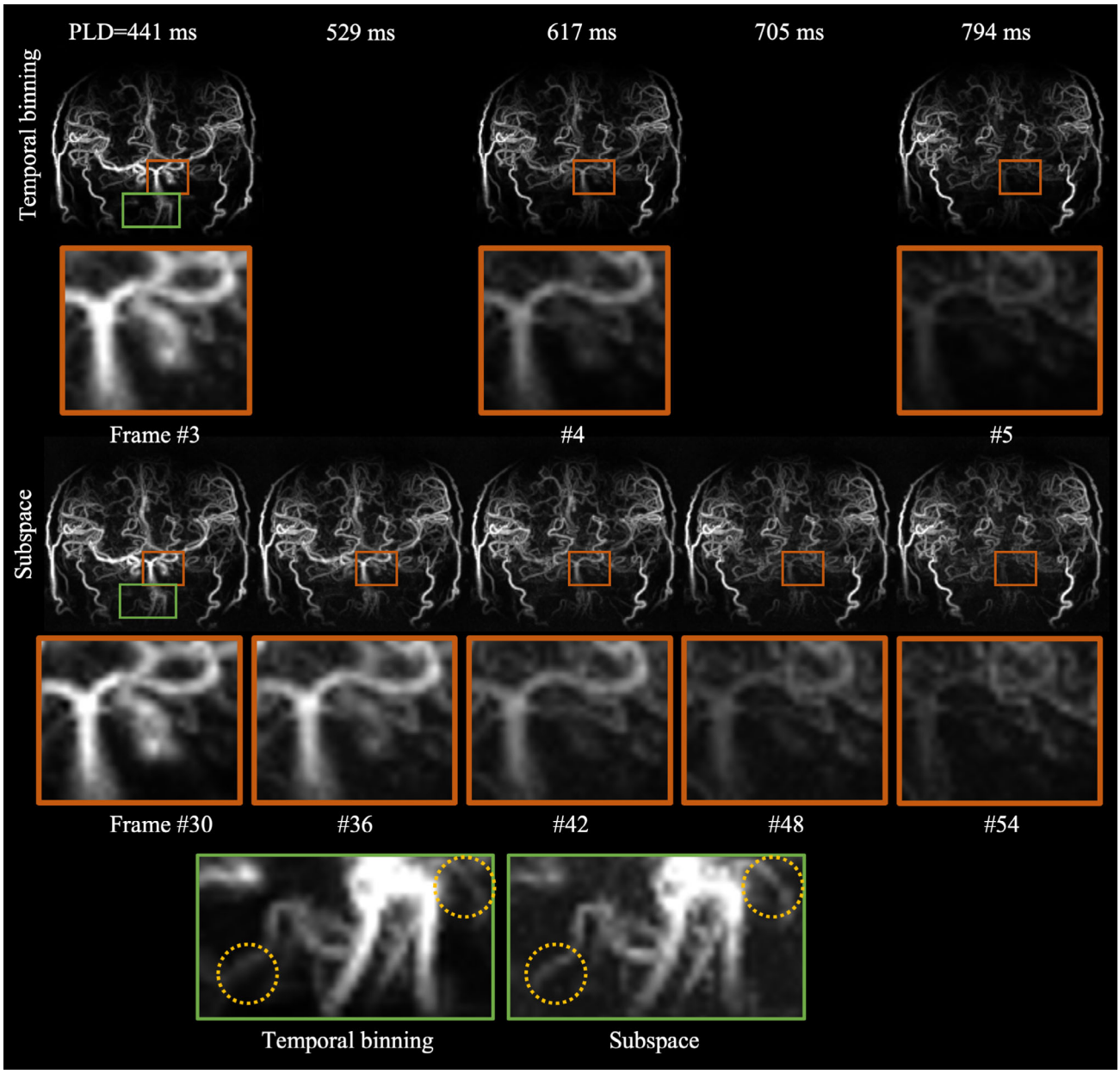

FIGURE 6 Comparison of in vivo dynamic MRA acquired with a cone trajectory and reconstructed by subspace and temporal binning methods at different post labeling delay times. Three of 12 frames reconstructed by temporal binning were shown on the top row. Similarly, among the 144 frames in total reconstructed by subspace method, five equispaced frames between 441 ms and 794 ms after labeling are also shown. Three of them matched the timepoints of the consecutive frames ~3–5 of temporal binning result. The blood flow dynamics shown in the zoomed-in regions demonstrated superior temporal discernibility of subspace method compared to temporal binning. The zoomed-in green box further showed evidence that the subspace method provided better clarity of vessels than temporal binning as highlighted by the yellow circles.

of the subspace reconstruction as could be seen from the enlarged green box. Overall, the subspace results demonstrated the best temporal and spatial fidelity and resolution among these reconstruction methods.

4 | DISCUSSION

In this work, a subspace, generated by linearly compressing a kinetic model, was incorporated into the reconstruction of 4D dynamic angiograms to achieve ultra-high temporal resolution (14.7 ms) and improved spatiotemporal fidelity. Our proposed subspace reconstruction was optimized through numerical simulations, where the optimal number of subspace principal components was chosen to balance the relative fitting error and computational requirements. Simulations were also used to find the optimal regularization weight, which is challenging to do using in vivo data where there is no ground

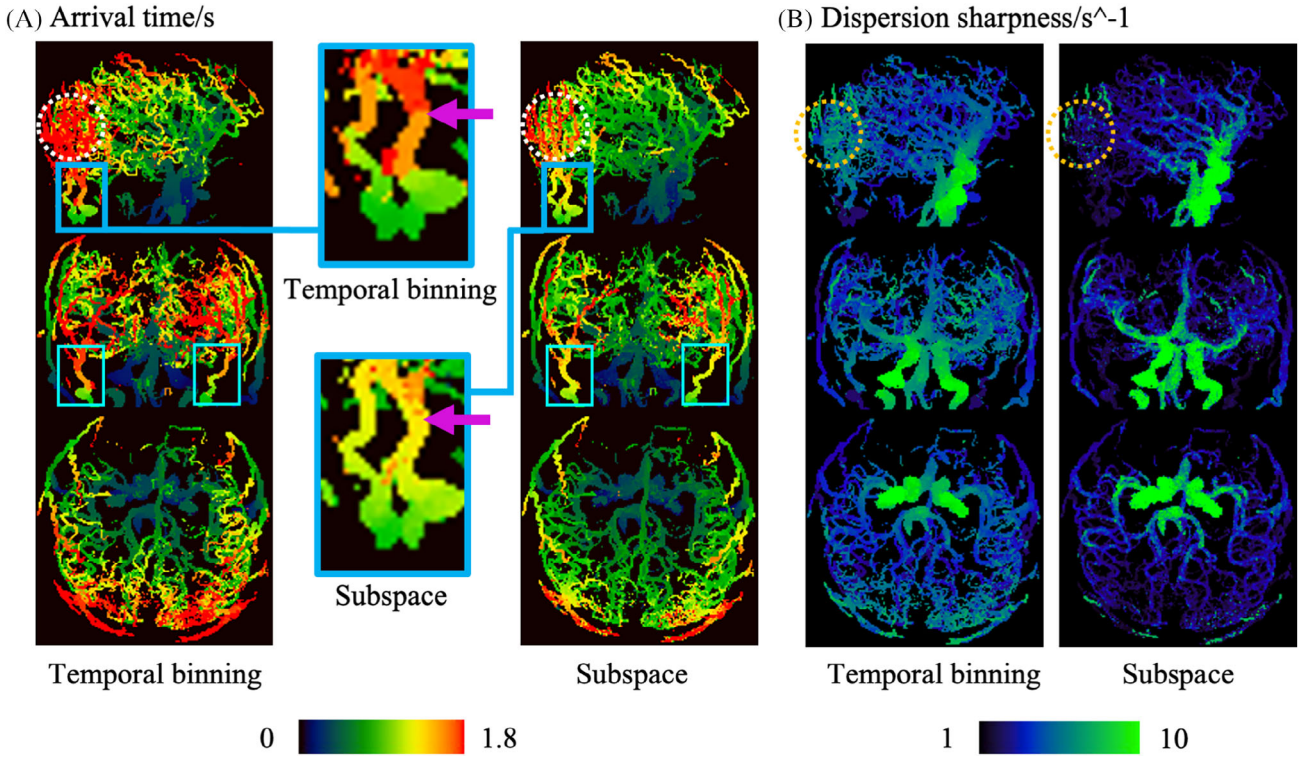

FIGURE 7 Comparison of blood arrival time and dispersion sharpness estimated from temporal binning and subspace results. (A) Arrival time in temporal binning MRA was overestimated and discontinuous (highlighted by the purple arrows), whereas that in subspace was smoother and more realistic. Asymmetry in the estimated arrival time of the temporal binning result in the external carotids (marked by the cyan box) was mitigated notably in the subspace result. (B) The dispersion sharpness estimated from temporal binning also demonstrated an increase in very distal vessels, which would not be expected as dispersion should continue to increase along the path of the vessels, whereas this effect was much less apparent in the subspace data. These results are consistent with the numerical phantom simulations shown in Figure 4.

truth. The reconstructed in vivo results were compared between the subspace and temporal binning methods and validated against the simulation results both qualitatively (improvement of spatiotemporal fidelity) and quantitatively (improvement of physiological modeling accuracy). Additionally, the proposed method was shown to outperform other advanced methods (LLR-matched and Extreme MRI[40]) when the same spatial and temporal resolution were used.

Incorporation of the modality specific prior knowledge (i.e., the kinetic model) was essential in obtaining ultra-high temporal resolution 4D angiograms without increasing scanning time (~6 min), because the high undersampling factor per frame presented a very ill-conditioned reconstruction problem. Alternative approaches that take advantage of compressed sensing[41] and adjusting the regularization weight could alleviate the problem of insufficient k-space sampling and artifacts from non-Cartesian trajectories[41–43] while also potentially introducing other artifacts (e.g., temporal blurring because of limiting the degrees of freedom on the temporal dimension). As shown in Figures S1 and S2, both LLR-matched and Extreme MRI[40] methods were evaluated with different regularization weights, and the results were either too noisy (i.e., under regularized) or too blurry (i.e., over regularized), with loss of distal vessel visibility. These results demonstrate that relying solely on locally low rank regularization limited the temporal variation to compensate for the insufficient sampling per frame and were not enough for faithful reconstruction of ultra-high temporal resolution 4D angiograms. In contrast, our subspace method incorporated a signal model of blood flow into the reconstruction, limiting the degrees of freedom. The fact that k-space samples acquired across the whole train of readouts can contribute to the estimation of each subspace coefficient map likely improves the spatial fidelity of the reconstruction. The subspace approach also avoids the temporal misallocation of signal that is inevitable in the temporal binning method. In our subspace method, a locally low rank regularization term was also included on the coefficient maps to reduce noise.

Several characteristics of the sequence used to acquire our data also contributed to achieving ultra-high temporal resolution 4D angiograms. First, the 3D golden angle[29] and repeat-first ordering[20] in the sequence guaranteed similar and approximately uniform k-space sampling at each

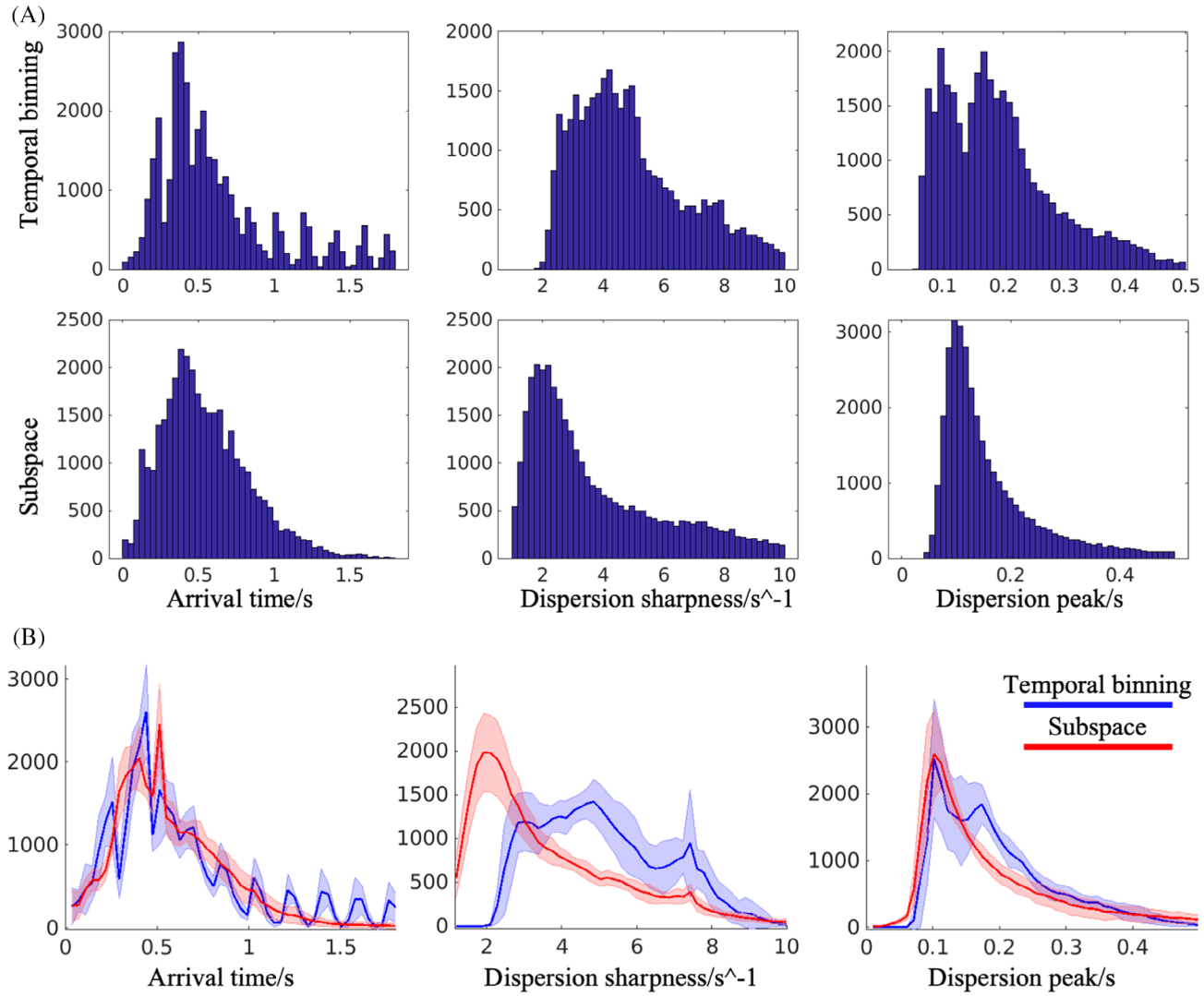

FIGURE 8 (A) Histogram of three angiography parameters estimated from one subject. (B) The distribution of these parameters on the group level. The average count of each value was plotted with the "red" and "blue" curves corresponding to subspace and temporal binning reconstruction methods, respectively. The SD of the voxel count across subjects was added as margins around the curve.

timepoint, which supported a frame window size of one TR in the subspace reconstruction. Voxels at different timepoints were also assumed to be spatially aligned for the kinetic model constraint to be applicable voxelwise. As the total readout time within each repeat is ~2 s, it is unlikely that significant motion will occur within each train of readouts. Because the between-repeat motion was shared for samples acquired across all TR periods, motion would be more likely manifested as blurriness rather than spatial misalignment between TRs, which is expected to make the subspace constrained reconstruction of 4D angiograms less motion sensitive.

Additionally, the proposed reconstruction was particularly advantageous for trajectories with lower sampling efficiency, such as 3D radial imaging, as can be seen from the simulation in Figure 3B. The poorer k-space coverage compared to the cone trajectory[26] means the radial approach benefits more from the effective sharing of information across timepoints that is achieved with a subspace reconstruction.

Compared to sliding window approaches like KWIC,[20–22] which reconstruct each frame independently with gridding, our method took advantage of the sampling across the whole train of readouts without timepoint mismatch between acquisition and reconstruction (i.e., signal from multiple TRs was combined for image of a single timepoint). Additionally, the LLR regularization applied on the subspace coefficient maps improved SNR in the final images, whereas the gridding approach used in KWIC would not provide additional denoising. Although a sliding window approach could be also combined with compress sensing to achieve additional noise suppression

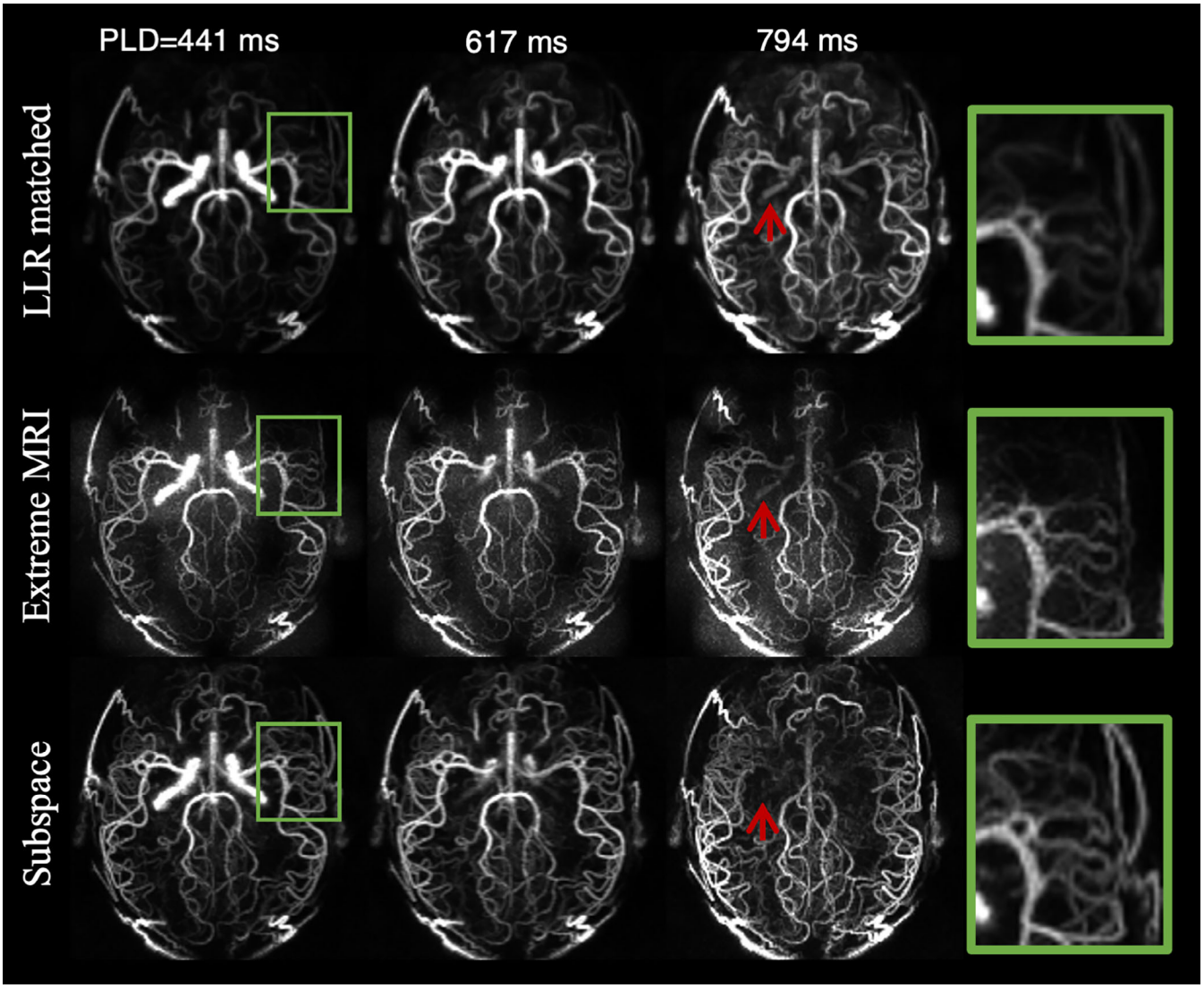

FIGURE 9 Comparison of subspace with other advanced reconstruction methods. LLR-matched adapted the temporal binning reconstruction to the same temporal resolution as subspace. Extreme MRI is a multi-scale low rank method and also had matched temporal resolution. Regions enlarged within the green box show loss of details in Extreme MRI and LLR-matched results, but better clarity in subspace. Red arrows highlighted falsely reconstructed arteries in LLR-matched because of regularization. Further investigation of the effects of regularization weight in Extreme MRI and LLR-matched is shown in Figures S1 and S2. LLR, locally low rank.

for high temporal resolution dynamic MRA, the computational requirements would be enormous. Compared to previously reported state-of-the-art work on 4D dynamic MRA, for which compromises had to be made either in temporal resolution[20] (1 mm^3 spatial resolution with ~100 ms temporal resolution) or in spatial resolution[11] (59 ms spatial resolution with 2-mm spatial resolution in slice direction), we achieved 1.1-mm isotropic spatial resolution, 14.7 ms temporal resolution, and 200 mm × 200 mm × 125 mm acquisition FOV within an ~6 min acquisition time. The full time series of subspace reconstructed MRA was exhibited in Figure S3 as a dynamic image. The corresponding coefficient maps were also shown in Figure S4. Although the 1.1-mm spatial resolution presented using the proposed subspace method is larger than the typical resolution of TOF angiography, the visibility of small vessels is potentially improved because the tissue background is suppressed much better in ASL compared to TOF.[11] In addition, the cone trajectory we used has the potential to achieve sub-millimeter resolution, providing much richer blood flow information than TOF spatially and temporally. The subspace method can also be significantly accelerated with GPUs and a faster optimization algorithm.

The proposed subspace reconstruction method could be extended to further improve the image quality of dynamic MRA. For instance, it could be combined with time-encoded PCASL to boost SNR by allowing for larger flip angle readouts and better background suppression.[18]

Incorporating the kinetic model informed reconstruction into such a protocol could combine the advantages of SNR and spatiotemporal resolution for better fidelity angiograms. An additional benefit of incorporating time-encoded PCASL is direct visualization of the in-flow of blood into the vasculature, which was not directly visible in our current implementation because of the long labeling duration, although inflow visualization can be achieved in postprocessing.[13]

The subspace approach could also incorporate the effects of B_1^+ variations. The simulated dictionary used to generate the subspace assumed a uniform B_1 field that holds approximately at 3 T. To further improve the reconstruction fidelity, especially at higher fields (e.g., 7 T), B_1^+ variations could be conveniently incorporated by simulating different sets of flip angles with various deviations from the expected ones when constructing the dictionary, enabling the proposed method to accommodate system imperfections.

Although the linear compression of the signal dictionary served as a close approximation for the true underlying signal model, there are several drawbacks to this approach. Modeling the angiography signal variation of the sequence in this work is complex as the labeled blood flows in the vessels while experiencing dispersion. Additionally, the in vivo transit time varied across a wide range from close to zero to longer than 1.8 s (according to our results), which is reflected as a temporal shift in the signal time series. Therefore, according to our simulations, 12 principal components were required to characterize 99.95% of signal variability in the dictionary. Further increasing the number of principal components gave marginal improvement in signal fitting, but increased the computational time and memory significantly. In addition, using more principal components would have weakened the prior constraint, potentially leading to increased noise sensitivity. In some extreme cases, where transit time was short or dispersion sharpness was large, the signal variation could not be represented accurately by the compressed subspace, contributing to errors in the reconstructed images. Non-linear methods like autoencoders[44] are capable of representing complex signal variations with a smaller number of independent components (i.e., in the latent space), as demonstrated by Arefeen et al.[45] However, the computational convenience brought by the permutation of linear operators would be lost, and the optimization would need to be performed with a subset of frames per iteration to accommodate limited memory. The balance between computational efficiency and representation accuracy remains to be explored in greater detail in future work.

Apart from the linearly compressed representation of the kinetic model being imperfect, the model itself might not be applicable to some complex flow scenarios present in patients. For example, modeling of the complex blood flow in an aneurysm is still the subject of ongoing research.[46] The kinetic model has proven to be applicable to abnormal flow patterns, like those found in Moyamoya disease.[13] For other cases like flow through arteriovenous malformations and turbulent flow within aneurysms, it is likely the dispersion parameters can accommodate some of these flow pattern variations. However, the actual generalizability of the subspace representation for the kinetic model to complex scenarios requires further investigation through testing in patient cohorts. However, the actual generalizability of the subspace representation for the kinetic model to complex scenarios requires further investigation through testing in patient cohorts.

Subspace-based dynamic perfusion images were not reconstructed because the signal acquired at early PLD is dominated by intravascular blood, which does not follow perfusion signal modeling. Angiographic model is a good approximation to the signal, especially at early PLDs, but the much weaker perfusion signal requires two models (i.e., angiographic and perfusion) to represent, which increases the complexity. Separate reconstruction of each signal requires further exploration in the future work.

In this preliminary study, a group of eight subjects was scanned to prove the feasibility and advantage of the proposed model informed reconstruction for accurate qualitative and quantitative assessment. Patients with cerebrovascular disease should be recruited and studied in the future for a more comprehensive examination of the effectiveness of our method. An effort could also be made to acquire ground truth data for the validation of the accuracy of the angiography quantification results obtained from the proposed reconstruction (e.g., using a very long scan time reference).

5 | CONCLUSION

In this work, we incorporated an angiographic kinetic model into the image reconstruction process and combined this with a subspace technique to achieve ultra-high temporal resolution 4D MRA. Our method took advantage of the prior knowledge of the angiographic signal timecourse to compensate for reduced sampling per frame and disentangled time-varying blood signal at different timepoints. The spatial and temporal fidelity of the resulting angiograms were, therefore, both notably improved. Parameter maps derived from the subspace results also benefited from the improved temporal fidelity and achieved better accuracy than that of the conventional temporally binned images in numerical simulation. Investigation on a group of healthy subjects demonstrated

superior image quality and angiography parameter quantification using the proposed subspace reconstruction compared to the temporal binning method, which is consistent with the simulation results.

ACKNOWLEDGMENTS

We are grateful for funding support from a Sir Henry Dale Fellowship jointly funded by the Wellcome Trust and the Royal Society (220204/Z/20/Z). The Wellcome Centre for Integrative Neuroimaging is supported by core funding from the Wellcome Trust (203139/Z/16/Z) with additional support from the National Institute for Health and Care Research (NIHR) Oxford Health Biomedical Research Centre (NIHR203316). W.W. is supported by the Royal Academy of Engineering (RF\201819\18\92). M.C. is supported by the Canada Research Chairs program. The views expressed are those of the authors and not necessarily those of the NIHR or the Department of Health and Social Care. Many thanks also to Jeff Fessler, Philipp Ehses, and colleagues for making available their excellent NUFFT and Siemens raw data reading MATLAB code, as well as to Siemens Healthineers for providing the base pulse sequence code, which we built on in this work. For the purpose of open access, the author has applied a CC BY public copyright license to any Author Accepted Manuscript version arising from this submission.

FUNDING INFORMATION

Sir Henry Dale Fellowship jointly funded by the Wellcome Trust and the Royal Society, Grant/Award Number, 220204/Z/20/Z; Wellcome Centre for Integrative Neuroimaging is supported by core funding from the Wellcome Trust, Grant/Award Numbers: 203139/Z/16/Z; National Institute for Health and Care Research (NIHR) Oxford Health Biomedical Research Centre, Grant/Award Number: NIHR203316; Royal Academy of Engineering, Grant/Award Number: RF\201819\18\92 to W.W.

CONFLICT OF INTEREST STATEMENT

This work builds on the original CAPRIA approach, which is the subject of a United States patent application on which T.W.O. is the sole author.

DATA AVAILABILITY STATEMENT

The code for cone trajectory used in this work could be found at https://github.com/Michaelsqj/TrajectoryDesign. The code for reconstruction and simulation could be found at https://github.com/Michaelsqj/dynamic_angio. The Fabber code for model fitting could be found at https://github.com/tomokell/fabber_models_asl/tree/capria. We are currently unable to share subject level data because of data protection issues, although our center is actively working on a solution to this.

ORCID

Qijia Shen https://orcid.org/0009-0009-1006-3869
Wenchuan Wu https://orcid.org/0000-0002-5020-5165
Mark Chiew https://orcid.org/0000-0001-6272-8783
Yang Ji https://orcid.org/0000-0003-4134-374X
Joseph G. Woods https://orcid.org/0000-0002-0329-824X
Thomas W. Okell https://orcid.org/0000-0001-8258-0659

REFERENCES

1. Saager C, Fitting T, Goebell E, Thomalla G, Fiehler J, Kucinski T. Contrast-enhanced MR angiography improves detection of carotid-T occlusion by acute stroke MRI. *Clin Neuroradiol*. 2008;18:163-167. doi:10.1007/s00062-008-8020-x
2. Bednarz G, Downes B, Werner-Wasik M, Rosenwasser RH. Combining stereotactic angiography and 3D time-of-flight magnetic resonance angiography in treatment planning for arteriovenous malformation radiosurgery. *Int J Radiat Oncol Biol Phys*. 2000;46:1149-1154. doi:10.1016/S0360-3016(99)00530-1
3. Willinek WA, von Falkenhausen M, Born M, et al. Noninvasive detection of steno-occlusive disease of the supra-aortic arteries with three-dimensional contrast-enhanced magnetic resonance angiography: a prospective, intra-individual comparative analysis with digital subtraction angiography. *Stroke*. 2005;36:38-43. doi:10.1161/01.STR.0000149616.41312.00
4. Kimia R, Elden L, Dailey J, et al. Magnetic resonance angiography (MRA) in preoperative planning for patients with 22q11.2 deletion syndrome undergoing craniofacial and otorhinolaryngologic procedures. *Int J Pediatr Otorhinolaryngol*. 2020;138:110236. doi:10.1016/j.ijporl.2020.110236
5. McDonald RJ, Levine D, Weinreb J, et al. Gadolinium retention: a research roadmap from the 2018 NIH/ACR/RSNA workshop on gadolinium chelates. *Radiology*. 2018;289:517-534. doi:10.1148/radiol.2018181151
6. Layne KA, Dargan PI, Archer JRH, Wood DM. Gadolinium deposition and the potential for toxicological sequelae – a literature review of issues surrounding gadolinium-based contrast agents. *Br J Clin Pharmacol*. 2018;84:2522-2534. doi:10.1111/bcp.13718
7. Burke LMB, Ramalho M, AlObaidy M, Chang E, Jay M, Semelka RC. Self-reported gadolinium toxicity: a survey of patients with chronic symptoms. *Magn Reson Imaging*. 2016;34:1078-1080. doi:10.1016/j.mri.2016.05.005
8. Ye Y, Hu J, Wu D, Haacke EM. Noncontrast-enhanced magnetic resonance angiography and venography imaging with enhanced angiography. *J Magn Reson Imaging*. 2013;38:1539-1548. doi:10.1002/jmri.24128
9. Dai W, Garcia D, de Bazelaire C, Alsop DC. Continuous flow-driven inversion for arterial spin labeling using pulsed radio frequency and gradient fields. *Magn Reson Med*. 2008;60:1488-1497. doi:10.1002/mrm.21790
10. Nishimura DG, Macovski A, Pauly JM, Conolly SM. MR angiography by selective inversion recovery. *Magn Reson Med*. 1987;4:193-202. doi:10.1002/mrm.1910040214
11. Okell TW, Schmitt P, Bi X, et al. Optimization of 4D vessel-selective arterial spin labeling angiography using

balanced steady-state free precession and vessel-encoding. *NMR Biomed*. 2016;29:776-786. doi:10.1002/nbm.3515
12. Uchino H, Ito M, Fujima N, et al. A novel application of four-dimensional magnetic resonance angiography using an arterial spin labeling technique for noninvasive diagnosis of Moyamoya disease. *Clin Neurol Neurosurg*. 2015;137:105-111. doi:10.1016/j.clineuro.2015.07.003
13. Okell TW, Chappell MA, Schulz UG, Jezzard P. A kinetic model for vessel-encoded dynamic angiography with arterial spin labeling. *Magn Reson Med*. 2012;68:969-979. doi:10.1002/mrm.23311
14. Plas MCE, Schmid S, Versluis MJ, Okell TW, Osch MJP. Time-encoded golden angle radial arterial spin labeling: simultaneous acquisition of angiography and perfusion data. *NMR Biomed*. 2021;34:e4519. doi:10.1002/nbm.4519
15. Wells JA, Lythgoe MF, Gadian DG, Ordidge RJ, Thomas DL. In vivo Hadamard encoded continuous arterial spin labeling (H-CASL). *Magn Reson Med*. 2010;63:1111-1118. doi:10.1002/mrm.22266
16. Teeuwisse WM, Schmid S, Ghariq E, Veer IM, van Osch MJP. Time-encoded pseudocontinuous arterial spin labeling: basic properties and timing strategies for human applications. *Magn Reson Med*. 2014;72:1712-1722. doi:10.1002/mrm.25083
17. Suzuki Y, Helle M, Koken P, Van Cauteren M, van Osch MJ. Simultaneous acquisition of perfusion image and dynamic MR angiography using time-encoded pseudo-continuous ASL. *Magn Reson Med*. 2018;79:2676-2684.
18. Woods JG, Schauman SS, Chiew M, Chappell MA, Okell TW. Time-encoded pseudo-continuous arterial spin labeling: increasing SNR in ASL dynamic angiography. *Magn Reson Med*. 2023;89:1323-1341. doi:10.1002/mrm.29491
19. Okell TW. Combined angiography and perfusion using radial imaging and arterial spin labeling. *Magn Reson Med*. 2019;81:182-194. doi:10.1002/mrm.27366
20. Song HK, Yan L, Smith RX, et al. Noncontrast enhanced four-dimensional dynamic MRA with golden angle radial acquisition and k-space weighted image contrast (KWIC) reconstruction: noncontrast enhanced radial 4D dMRA. *Magn Reson Med*. 2014;72:1541-1551. doi:10.1002/mrm.25057
21. Song HK, Dougherty L. k-space weighted image contrast (KWIC) for contrast manipulation in projection reconstruction MRI. *Magn Reson Med*. 2000;44:825-832. doi:10.1002/1522-2594(200012)44:6<825::AID-MRM2>3.0.CO;2-D
22. Chen Z, Zhou Z, Qi H, et al. A novel sequence for simultaneous measurement of whole-brain static and dynamic MRA, intracranial vessel wall image, and T_1-weighted structural brain MRI. *Magn Reson Med*. 2021;85:316-325. doi:10.1002/mrm.28431
23. Parmar H, Ivancevic MK, Dudek N, Gandhi D, Mukherji SK. Dynamic MRA with four-dimensional time-resolved angiography using keyhole at 3 tesla in head and neck vascular lesions. *J Neuroophthalmol*. 2009;29:119-127. doi:10.1097/WNO.0b013e3181a58c20
24. pei LZ. Spatiotemporal IMAGINGWITH partially separable functions. *2007 4th IEEE International Symposium on Biomedical Imaging: From Nano to Macro*; IEEE; 2007:988-991. doi:10.1109/ISBI.2007.357020
25. Tamir JI, Uecker M, Chen W, et al. T_2 shuffling: sharp, multicontrast, volumetric fast spin-echo imaging. *Magn Reson Med*. 2017;77:180-195. doi:10.1002/mrm.26102
26. Shen Q, Wu W, Chiew M, Ji Y, Woods JG, Okell TW. Efficient 3D cone trajectory design for improved combined angiographic and perfusion imaging using arterial spin labeling. *Magn Reson Med*. 2024;92:1568-1583. doi:10.1002/mrm.30149
27. Okell TW, Chiew M. Optimization of 4D combined angiography and perfusion using radial imaging and arterial spin labeling. *Magn Reson Med*. 2023;89:1853-1870. doi:10.1002/mrm.29558
28. Okell TW, Woods JG, Chiew M. Combined angiographic, structural and perfusion radial imaging using arterial spin labeling. *Proceedings 25th Scientific Meeting; ISMRM*; 2022:341.
29. Chan RW, Ramsay EA, Cunningham CH, Plewes DB. Temporal stability of adaptive 3D radial MRI using multidimensional golden means. *Magn Reson Med*. 2009;61:354-363. doi:10.1002/mrm.21837
30. Winkelmann S, Schaeffter T, Koehler T, Eggers H, Doessel O. An optimal radial profile order based on the Golden ratio for time-resolved MRI. *IEEE Trans Med Imaging*. 2007;26:68-76. doi:10.1109/TMI.2006.885337
31. Trzasko J, Manduca A. Local versus global low-rank promotion in dynamic MRI series reconstruction. *Proceedings 19th Scientific Meeting*; 2011:4371.
32. Fessler JA. Michigan Image Reconstruction Toolbox. 2013. Accessed September 1, 2023. http://web.eecs.umich.edu/~fessler/irt/irt
33. Ehses P. mapVBVD. 2022. Accessed September 1, 2023. https://github.com/pehses/mapVBVD
34. Fessler J. Image Reconstruction Toolbox. 2015. Accessed September 1, 2023. http://web.eecs.umich.edu/~fessler/irt
35. Fessler JA, Sutton BP. Nonuniform fast fourier transforms using min-max interpolation. *IEEE Trans Signal Process*. 2003;51:560-574. doi:10.1109/TSP.2002.807005
36. Chappell MA, Groves AR, Whitcher B, Woolrich MW. Variational Bayesian inference for a nonlinear forward model. *IEEE Trans Signal Process*. 2009;57:223-236. doi:10.1109/TSP.2008.2005752
37. Jenkinson M, Beckmann CF, Behrens TEJ, Woolrich MW, Smith SM. FSL. *NeuroImage*. 2012;62:782-790. doi:10.1016/j.neuroimage.2011.09.015
38. Buehrer M, Pruessmann KP, Boesiger P, Kozerke S. Array compression for MRI with large coil arrays. *Magn Reson Med*. 2007;57:1131-1139. doi:10.1002/mrm.21237
39. Walsh DO, Gmitro AF, Marcellin MW. Adaptive reconstruction of phased array MR imagery. *Magn Reson Med*. 2000;43:682-690. doi:10.1002/(SICI)1522-2594(200005)43:5<682::AID-MRM10>3.0.CO;2-G
40. Ong F, Zhu X, Cheng JY, et al. Extreme MRI: large-scale volumetric dynamic imaging from continuous non-gated acquisitions. *Magn Reson Med*. 2020;84:1763-1780. doi:10.1002/mrm.28235
41. Lustig M, Donoho D, Pauly JM. Sparse MRI: the application of compressed sensing for rapid MR imaging. *Magn Reson Med*. 2007;58:1182-1195. doi:10.1002/mrm.21391
42. Pruessmann KP, Weiger M, Börnert P, Boesiger P. Advances in sensitivity encoding with arbitrary k-space trajectories. *Magn Reson Med*. 2001;46:638-651. doi:10.1002/mrm.1241
43. Block KT, Uecker M, Frahm J. Undersampled radial MRI with multiple coils. Iterative image reconstruction using a total variation constraint. *Magn Reson Med*. 2007;57:1086-1098. doi:10.1002/mrm.21236

44. Bank D, Koenigstein N, Giryes R. Autoencoders. 2021. doi:10.48550/arXiv.2003.05991
45. Arefeen Y, Xu J, Zhang M, et al. Latent signal models: learning compact representations of signal evolution for improved time-resolved, multi-contrast MRI. *Magn Reson Med*. 2023;90:483-501. doi:10.1002/mrm.29657
46. Sforza DM, Putman CM, Cebral JR. Hemodynamics of cerebral aneurysms. *Annu Rev Fluid Mech*. 2009;41:91-107. doi:10.1146/annurev.fluid.40.111406.102126

SUPPORTING INFORMATION

Additional supporting information may be found in the online version of the article at the publisher's website.

Figure S1. Angiograms reconstructed by Extreme MRI with different regularization weights. Low regularization weight kept the fidelity of angiography but lost SNR, whereas high regularization weight overly smoothed the image and lost visibility of thin vessels, as indicated by the yellow circles. Arteries pointed by the red arrows also appeared at late timepoints only at high regularization weight, confirming these were artifacts introduced due to over-regularized on the temporal dimension.

Figure S2. Angiography reconstructed by "LLR-matched" with different regularization weights. In a similar way to Extreme MRI, the choice of regularization weight for LLR matched was a compromise between excessive smoothing and noisy images.

Figure S3. An example movie of dynamic MRA reconstructed by the subspace method shows smooth blood flow into the brain. The contrast of each frame was separately adjusted for clarity. From left to right: Maximum intensity projection (MIP) in Sagittal, coronal and transverse view.

Figure S4. The 12 coefficient maps corresponding to 12 extracted principal components.

Table S1. Acquisition parameters for the three different in vivo protocols.

How to cite this article: Shen Q, Wu W, Chiew M, Ji Y, Woods JG, Okell TW. Ultra-high temporal resolution 4D angiography using arterial spin labeling with subspace reconstruction. *Magn Reson Med*. 2025;93:1924-1941. doi: 10.1002/mrm.30407